photonics

MDPI

Article

Multi-Objective Optimization of Space Camera Primary Mirror Structure Based on Dynamic Constraint SHAMODE Algorithm

Jiaheng Tan [1,2], Wei Xu [1,2], Shuangtong Zhu [1], Lin Chang [1] and Qiang Yong [1,*]

[1] Changchun Institute of Optics, Fine Mechanics and Physics, Chinese Academy of Sciences, Changchun 130033, China; tanjiaheng22@mails.ucas.ac.cn (J.T.)
[2] University of Chinese Academy of Sciences, Beijing 100049, China
* Correspondence: yongqiang@ciomp.ac.cn; Tel.: +86-15044164780

Abstract

Aiming at the structural lightweight design of a 700 mm aperture primary mirror for a space camera, a novel success history-based adaptive multi-objective differential evolution algorithm with dynamic constraint handling is proposed to solve the multi-objective optimization problem of simultaneously minimizing mass and compliance under strict constraints for surface error and first-order modal frequency. Firstly, a surrogate model for the mirror was constructed using the Kriging algorithm based on Optimal Latin Hypercube Sampling, establishing a mapping relationship between input design variables and output responses, thereby replacing computationally expensive finite element simulations. Subsequently, a dynamic constraint adjustment mechanism was introduced into the Success History-based Adaptive Multi-Object Differential Evolution algorithm for the surrogate model, dynamically relaxing and tightening constraint violation requirements during iteration. This allows for utilizing promising yet infeasible solutions for rapid convergence while ensuring the feasibility of the final solutions. Comparisons with 13 advanced constrained multi-objective optimization algorithms demonstrate that the proposed algorithm exhibits excellent convergence, diversity, and consistency. Finally, the optimal solution was selected from the Pareto front obtained by the proposed algorithm, and the design variable values were adjusted according to manufacturing constraints to yield the final optimization result, which was then verified by finite element simulation. The simulation results show that the final mirror structure meets all performance constraints, demonstrating the effectiveness and engineering applicability of the proposed algorithm for the structural lightweight design of space camera mirrors.

Keywords: primary mirror; constrained multi-objective optimization algorithm; space camera; optimized design; lightweight structure

Check for updates

Received: 14 February 2026
Revised: 4 March 2026
Accepted: 9 March 2026
Published: 16 March 2026

Copyright: © 2026 by the authors. Licensee MDPI, Basel, Switzerland. This article is an open access article distributed under the terms and conditions of the Creative Commons Attribution (CC BY) license.

1. Introduction

As a crucial tool for human exploration of the universe and observation of the Earth, the imaging quality of a space camera directly determines the capability of acquiring scientific data and the success of missions. Compact, high-quality imaging systems are highly desired for scientific, industrial, and consumer applications [1]. With the rise of commercial aerospace and technological iteration, the demands for lightweight design and high imaging quality of space cameras are increasingly stringent. The mirror, as a key component of the optical system in a space camera, significantly impacts its imaging quality [2]. During ground manufacturing, testing, transportation, and other processes, the

mirror is subjected to its own gravity, and it also encounters disturbances from external environmental vibrations during rocket launch. Consequently, the mirror must possess high stiffness to ensure surface accuracy. Meanwhile, the launch capability and cost of rockets impose limitations on the mirror's mass. Therefore, balancing the mass and stiffness of the mirror under the premise of meeting surface accuracy requirements has become an important task in the optimal design of mirrors.

In recent years, scholars have conducted extensive research on the optimal design of space camera mirrors. Zhang et al. proposed a surrogate model based on a Bayesian regularization algorithm-based recurrent neural network for space camera mirrors and utilized the NSGA-II algorithm to optimize the surrogate model with objectives of minimizing weight, first-order modal frequency, and root mean square (RMS) of gravity-induced deformation [3]. Wang et al. applied a Backpropagation (BP) neural network to construct a surrogate model for a space-based large mirror structure to capture the nonlinear mapping between target characteristics and design variables in structural optimization design [4]. Liu et al. employed the compromise programming method to optimize the structural parameters of the primary mirror of a remote sensing camera, transforming multiple optimization objectives into a single objective [5]. Wang et al. optimized the mirror structure through experimental design and utilized the NSGA-II algorithm for multi-objective optimization of mirror parameters [6]. Liu et al. grouped the lightweight ribs of the mirror based on topology optimization results, then selected key factors through experimental design, and performed mirror parameter optimization with the objectives of minimizing the RMS of surface error and mass, and with the first-order modal frequency as a constraint [7]. Dong et al. proposed a multi-objective optimization design method for mirrors based on dual-parameter coupling, which improved upon the shortcomings of considering only single structural variations without accounting for other factors [8]. Sun et al. adopted a MATLAB (R2017a)-Python (Version 3.4.0)-Abaqus (Version 6.9) co-simulation to avoid the inefficiency of manually changing structural parameters and combined it with a non-dominated sorting genetic algorithm to achieve integrated optimization of the entire mirror's structural parameters [9]. Qin et al., addressing the high computational cost of optomechanical simulation, proposed a surrogate model based on a hybrid of improved particle swarm optimization (IPSO), adaptive genetic algorithm (IAGA), and optimized back propagation neural network (IPSO-IAGA-BPNN), and combined it with MOEAs to propose a Pareto-optimal primary mirror design method [10].

Existing research on mirror optimization design has predominantly focused on establishing surrogate models for mirrors or converting multiple optimization objectives into a single objective for optimization. There has been relatively less discussion on multi-objective optimization algorithms, with classical algorithms such as NSGA-II or MOEA/D commonly employed. Currently, evolutionary algorithms have become mainstream methods for solving multi-objective optimization problems due to their excellent performance in global search and parallel processing [11]. Tian et al. proposed an adaptive population size method that dynamically shrinks the auxiliary population based on the current evolutionary state and on this basis proposed a multi-stage evolutionary algorithm that saves computational resources [12]. Ming et al. proposed a dual-population-based evolutionary algorithm called c-DPEA, which maintains an appropriate balance between convergence and diversity through two collaborative and complementary populations [13]. Ban et al. proposed a decision variable classification method that categorizes variables into constraint-related and constraint-unrelated variables based on their relationship with constraints. By independently optimizing these two types of variables, fast convergence is achieved while maintaining population diversity [14]. Ming et al. proposed a constrained penalty boundary intersection (CPBI) method and applied it to a decomposition-based multi-objective

evolutionary algorithm to simultaneously optimize convergence, diversity, and feasibility [15]. Additionally, some competitive multi-objective optimization algorithms include EMCMMS [16], EMCMO [17], CMOEACD [18], CGMEA [19], FSM-CMO [20], among others. Despite their individual strengths, the No Free Lunch Theorem [21] suggests that strong performance on a particular class of problems does not imply similar effectiveness across different problem domains. Consequently, no universal algorithm exists for all optimization tasks, which underscores the necessity of designing new algorithms tailored to mirror structural parameter optimization.

Building on previous research, this paper conducts a structural parameter optimization study for a 700 mm aperture primary mirror of a space camera. Firstly, parametric modeling of the mirror structure is performed to establish a finite element model and construct an integrated simulation linkage for the mirror. Subsequently, a surrogate model for the mirror is established using the Kriging algorithm through optimal Latin hypercube sampling. For the surrogate model, a success history-based adaptive multi-objective differential evolution algorithm (SHAMODE) with dynamic constraints is proposed. SHAMODE is a high-performance improvement of the differential evolution algorithm [22]. In recent years, various multi-objective algorithm variants targeting structural optimization problems have been developed and demonstrated good performance [23–25]. Considering the characteristics of mirror structural parameter optimization, this paper effectively balances population convergence and diversity by introducing a constraint dynamic adjustment mechanism. The effectiveness of the proposed algorithm is validated through comparisons with thirteen established multi-objective optimization algorithms. Finite element analysis is conducted on the optimized mirror. Simulation results indicate that, compared to the initial mirror structure, the lightweight rate reaches 32.2% while ensuring surface accuracy and fundamental frequency requirements are met.

2. Problem Definition of Structural Optimization Design for Mirrors

2.1. Initial Structural Design of the Mirror

This paper focuses on the 700 mm aperture primary mirror of a space camera. Based on actual requirements and empirical formulas, a semi-open lightweight mirror back is adopted as the initial design of the mirror. The interior of the mirror features traditional triangular lightweight holes, including three support holes and a pentagonal central hole. The initial structure of the mirror is shown in Figure 1.

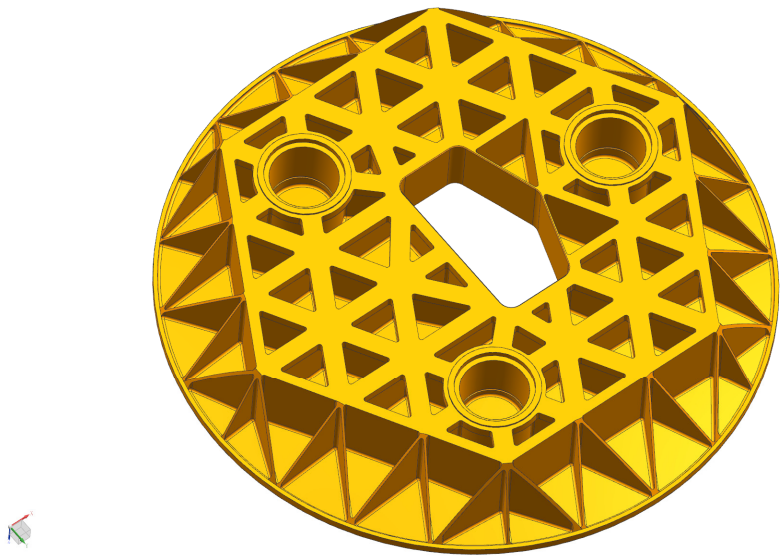


Figure 1. The initial structure of the primary mirror.

Currently, the main materials used for optical components in space camera mirrors include ultra-low expansion glass (ULE), silicon carbide (SiC), zero thermal expansion glass-ceramic (Zerodur), and metallic beryllium (Be) [26,27]. The properties of these optical materials are listed in Table 1. During the in-orbit operation of a space camera, the external heat flux and internal heat source conditions continuously change. Matching the thermal expansion coefficient of materials is one of the primary considerations when selecting materials for the primary mirror assembly. Therefore, this paper selects silicon carbide, which possesses high specific stiffness, high thermal conductivity, and a low coefficient of thermal expansion, as the material for the mirror.

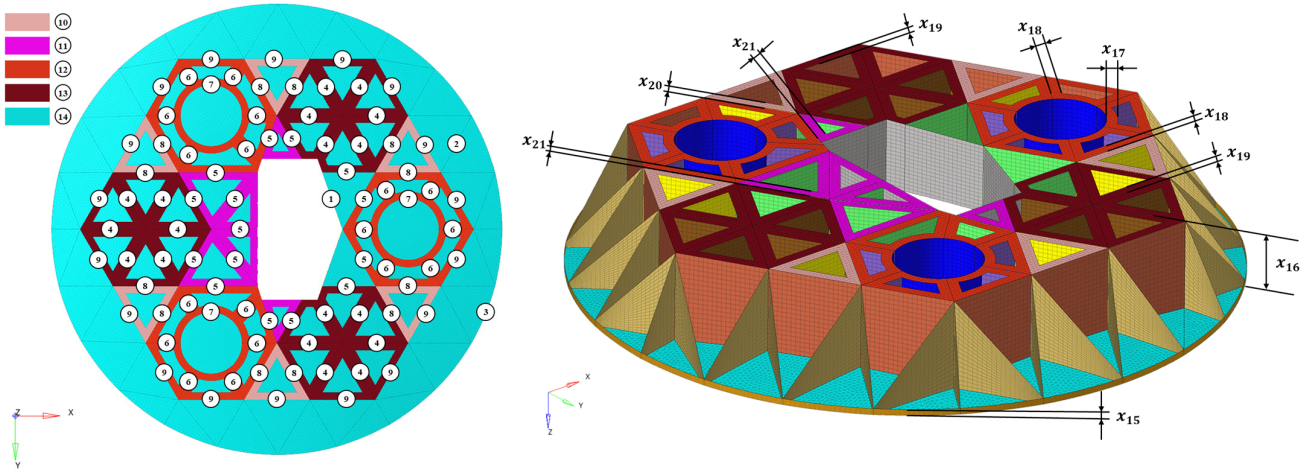
Table 1. Optical material properties.

Property *	SiC	ULE	Zerodur	Be
Elastic modulus	400	67	91	287
Density	3200	2210	2530	1850
Thermal expansion coefficient	2.4	0.03	0.05	11.4
Thermal conductivity	155	1.31	1.64	216

* Elastic modulus is in GPa; density is in $kg \cdot m^{-3}$; thermal expansion coefficient is in $10^{-6} \cdot K^{-1}$; thermal conductivity is in $W \cdot K^{-1} \cdot m^{-1}$.

2.2. Definition of Design Variables and Multi-Objective Optimization Problem

A two-dimensional shell element finite element model of the initial mirror structure was established using HyperMesh (Altair Engineering Inc., version 2017, Troy, MI, USA), consisting of 98,062 shell elements and 73,063 nodes (The finite element model is provided in the Supplementary Materials). Based on the structural symmetry and load transfer characteristics, the finite element model was divided into 14 groups of thickness variables and 7 groups of shape variables for optimization design. The thickness variables control the thickness of the vertical ribs, the back semi-open ribs, and the mirror face, as shown in Figure 2a. The shape variables control the width of the back semi-open ribs, the height of the outer ring ribs, and the overall height, as shown in Figure 2b. Additionally, the dimensional ranges of all design variables were determined based on manufacturing constraints. The initial values of each design variable and their corresponding dimensional ranges are listed in Table 2.



(**a**) (**b**)

Figure 2. Schematic diagrams of variable grouping (**a**) Thickness variables; (**b**) Shape variables.

Table 2. Initial mirror structure parameters and variation ranges.

Name	Parameter *	Initial Value/mm	Lower Value/mm	Upper Value/mm
Central hole wall thickness	x_1	2.5	2.0	6.0
Chamfered edge vertical ribs thickness	x_2	2.5	2.0	6.0
Outer ring ribs thickness	x_3	2.5	2.0	6.0
Supported hole symmetric position radial ribs thickness	x_4	2.5	2.0	6.0
Central hole adjacent vertical ribs thickness	x_5	2.5	2.0	6.0
Supported hole radial ribs thickness	x_6	2.5	2.0	6.0
Supported hole wall thickness	x_7	2.5	2.0	6.0
Medial vertical ribs thickness	x_8	2.5	2.0	6.0
Lateral vertical ribs thickness	x_9	2.5	2.0	6.0
Medial back semi-open ribs thickness	x_{10}	12.0	3.0	15.0
Central hole adjacent back semi-open ribs thickness	x_{11}	12.0	3.0	15.0
Supported hole adjacent back semi-open ribs thickness	x_{12}	12.0	3.0	15.0
Supported hole symmetric position back semi-open ribs thickness	x_{13}	12.0	3.0	15.0
Mirror surface thickness	x_{14}	5.0	3.0	8.0
Outer ring ribs height	x_{15}	10.0	10.0	110.0
Overall vertical ribs height	x_{16}	110.0	60.0	135.0
Supported hole back semi-open ribs width	x_{17}	10.0	5.0	15.0
Supported hole adjacent back semi-open ribs width	x_{18}	10.0	5.0	15.0
Supported hole symmetric position back semi-open ribs width	x_{19}	10.0	5.0	15.0
Medial back semi-open ribs width	x_{20}	10.0	5.0	15.0
Central hole adjacent back semi-open ribs width	x_{21}	10.0	5.0	15.0

* Design variables x_1~x_9 represent the thickness parameters of different vertical ribs at the corresponding numbered positions in Figure 2a, x_{10}~x_{14} denote the thickness parameters of various back semi-open ribs and the mirror surface with corresponding colors in Figure 2a. Design variables x_{15} and x_{16} represent the height parameters of two types of vertical ribs, while x_{17}~x_{21} denote the width parameters of different back semi-open ribs, as shown in Figure 2b.

Subsequently, MSC.Nastran (Hexagon AB, MD Nastran r3, Stockholm, Sweden) was used to perform a static analysis on the mirror. Fixed constraints were applied to nodes on all supported hole walls via 6-DOF SPCs, and external loads of 1 g gravity were imposed along the x, y, and z directions respectively to analyze the self-weight deformation and displacement of the mirror in the three directions. Rigid-body displacement was then removed using SigFit (Sigmadyne Inc., version 2010R2D, Rochester, NY, USA) to calculate the surface error root mean square (RMS) and peak-to-valley (PV) values of the mirror under 1 g gravity along the x, y, and z directions. Furthermore, OptiStruct (Altair Engineering Inc., version 2017, Troy, MI, USA) was employed to conduct a modal analysis on the mirror with the same constraints as in the static analysis, so as to obtain the mass, first-order natural frequency, and compliance (in the x, y, and z directions) of the mirror.

The optical performance and first-order mode shape of the initial mirror structure are shown in Figure 3. The RMS_x is 2.9552 nm, PV_x is 13.026 nm, RMS_y is 3.0947 nm,

PV_y is 14.732 nm, RMS_z is 12.567 nm, PV_z is 47.487 nm, the first-order modal frequency is 2306.889 Hz, and the mass of the initial mirror structure is 16.8105 kg.

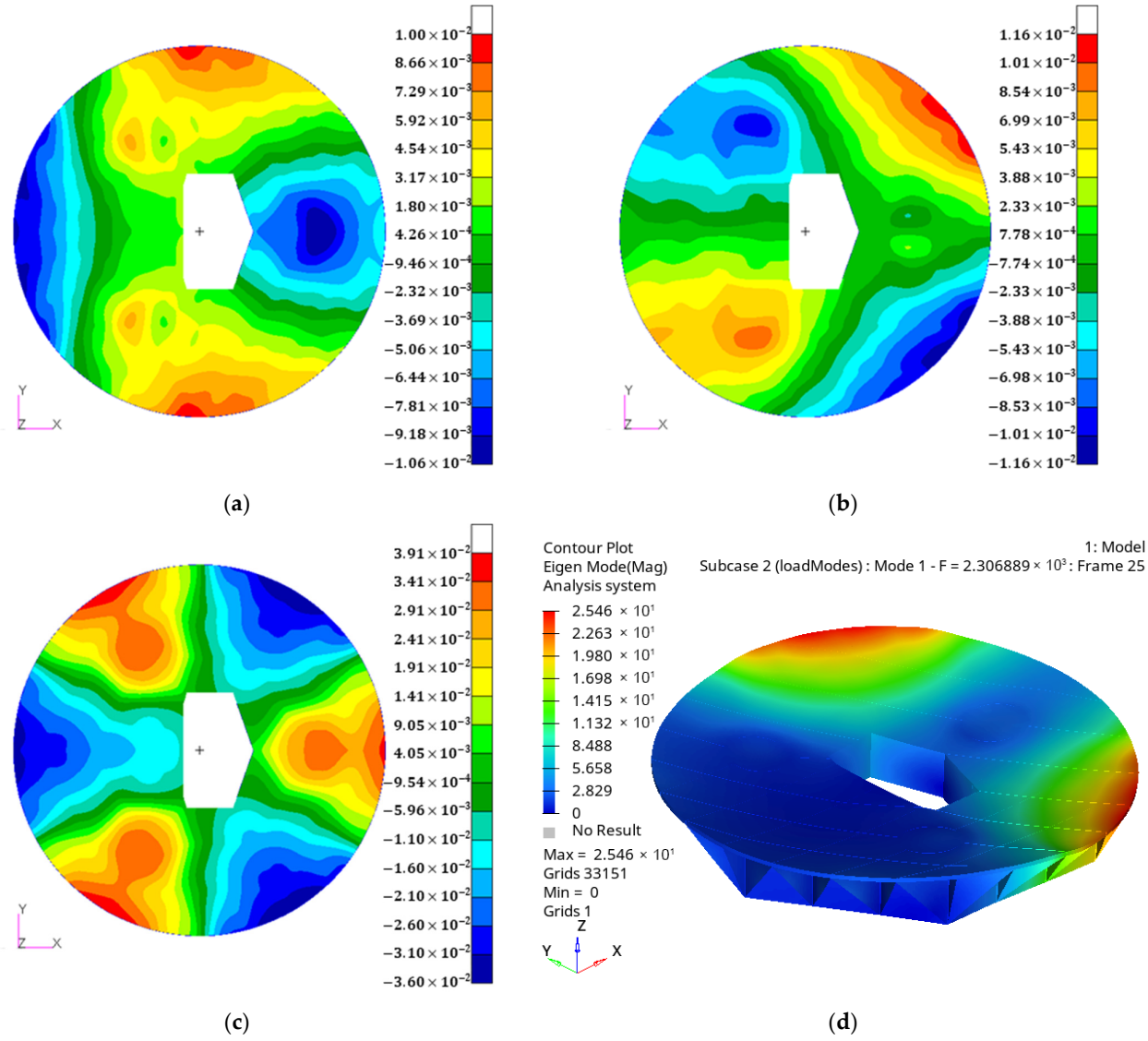


Figure 3. (**a**) Surface error of the initial mirror structure in the x-direction; (**b**) Surface error of the initial mirror structure in the y-direction; (**c**) Surface error of the initial mirror structure in the z-direction; (**d**) First-order mode shape of the initial mirror structure.

According to the performance specifications, the surface error RMS values of the mirror under 1 g gravity in the x, y, and z directions must be less than λ/50, and the PV values must be less than λ/10 (λ = 632.8 nm). Simultaneously, the first-order modal frequency must be greater than 2000 Hz to prevent resonance. Although the initial mirror structure designed based on empirical formulas can meet the performance requirements, it may not represent the global optimal solution. Therefore, this paper takes the minimization of the average compliance in the x, y, and z directions and the minimization of mass as the two objective functions for optimization. The multi-objective optimization problem for the mirror's structural parameters can be formulated as:

$$\min f(\boldsymbol{x}) = (f_1(\boldsymbol{x}), f_2(\boldsymbol{x})), \tag{1}$$

$$\text{s.t.}\begin{cases} f_1(\boldsymbol{x}) = Mass(\boldsymbol{x}), \\ f_2(\boldsymbol{x}) = \left(Compliance_x(\boldsymbol{x}) + Compliance_y(\boldsymbol{x}) + Compliance_z(\boldsymbol{x})\right)/3, \\ g_1(\boldsymbol{x}) = RMS_x(\boldsymbol{x}) - 1.2656 \times 10^{-5} \le 0, \\ g_2(\boldsymbol{x}) = RMS_y(\boldsymbol{x}) - 1.2656 \times 10^{-5} \le 0, \\ g_3(\boldsymbol{x}) = RMS_z(\boldsymbol{x}) - 1.2656 \times 10^{-5} \le 0, \\ g_4(\boldsymbol{x}) = PV_x(\boldsymbol{x}) - 6.328 \times 10^{-5} \le 0, \\ g_5(\boldsymbol{x}) = PV_y(\boldsymbol{x}) - 6.328 \times 10^{-5} \le 0, \\ g_6(\boldsymbol{x}) = PV_z(\boldsymbol{x}) - 6.328 \times 10^{-5} \le 0, \\ g_7(\boldsymbol{x}) = 2000 - Frequence_{1st}(\boldsymbol{x}) \le 0, \end{cases} \tag{2}$$

where $f(\boldsymbol{x})$ represents the objective function that needs to be minimized, $\boldsymbol{x} = (x_1, x_2, \ldots, x_{21})^T$ represents the vector of the grouped mirror structural design variables (mm). $Mass(\boldsymbol{x})$ denotes the mass (kg), $Compliance_x(\boldsymbol{x})$, $Compliance_y(\boldsymbol{x})$, and $Compliance_z(\boldsymbol{x})$ represent the compliance (N·mm) in the x, y, and z directions respectively, $RMS_x(\boldsymbol{x})$, $RMS_y(\boldsymbol{x})$, and $RMS_z(\boldsymbol{x})$ denote the RMS values (mm) of the surface error under 1 g gravity in the x, y, and z directions respectively, $PV_x(\boldsymbol{x})$, $PV_y(\boldsymbol{x})$, and $PV_z(\boldsymbol{x})$ denote the PV values (mm) of the surface figure error under 1 g gravity in the x, y, and z directions respectively, and $Frequence_{1st}(\boldsymbol{x})$ represents the first-order modal frequency (Hz).

2.3. Integrated Simulation Linkage and Surrogate Model Construction

Since optimization design requires frequent modification of design variables and examination of corresponding analysis results, constructing a surrogate model to capture the mapping relationship between input design variables and output responses can replace actual finite element simulations, significantly reducing the computational time and resources required [28]. As the foundation for building a surrogate model, the quantity and quality of training samples have a significant impact on the accuracy and generalization ability of the surrogate model. High-accuracy surrogate models typically require a large number of training samples, which can still lead to high computational costs. Therefore, to ensure sample representativeness while balancing prediction accuracy and computational cost, this paper employs the optimal Latin hypercube sampling (OLHS) [29] method within the design of experiment to generate a set of 2000 sample points uniformly distributed in the design space. Among these, 1600 points are randomly selected as the training set, and the remaining 400 serve as the test set for evaluating the prediction accuracy of the surrogate model.

To efficiently obtain the output responses for the 2000 sample points, this paper establishes an integrated simulation linkage for the mirror using Isight (Dassault Systèmes, version 4.0, Vélizy-Villacoublay, France). Based on the position of each sample point in the design space, this linkage automatically adjusts the corresponding structural parameters of the mirror and invokes analysis software to compute the corresponding output responses. The integrated simulation linkage is illustrated in Figure 4. For each sample point, the process begins by using the TCL command script file (generated by HyperMesh during the analysis of the initial mirror structure) as a template. The values controlling the design variable parameters are extracted and modified to create a new command script file. HyperMesh is then invoked to generate a finite element model with the new design variable parameters. Subsequently, OptiStruct is run to obtain the mirror's mass, compliance, and first-order modal frequency. Nastran is executed to calculate nodal displacements. SigFit is then used to compute the mirror's surface error after removing rigid-body displacement. Finally, the output response values are extracted and saved.

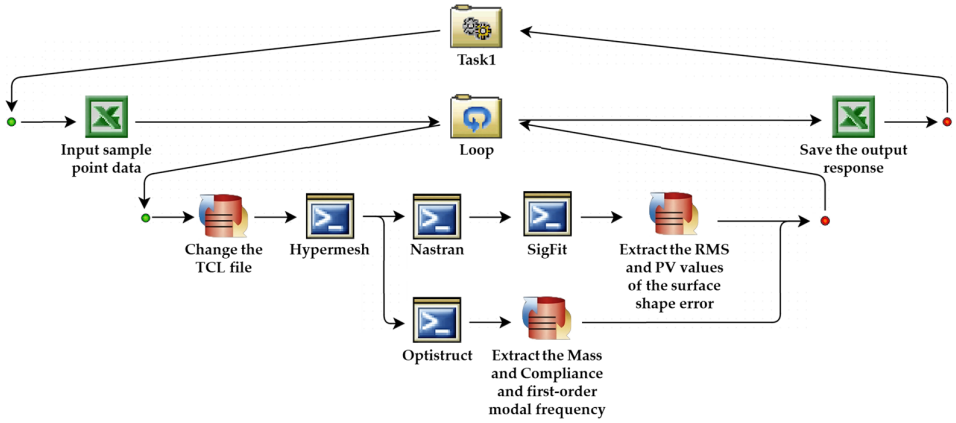


Figure 4. Mirror integrated simulation linkage.

Subsequently, based on the input design variables and output responses of the training set samples, a surrogate model for the mirror was constructed using the Kriging algorithm [30,31], employing a Gaussian correlation function and a quadratic polynomial trend function. The surrogate model was then used to predict the corresponding output responses for the input design variables of the test set samples. These predicted values were compared with the actual output responses obtained from the integrated simulation linkage. The prediction accuracy was evaluated using the Mean Absolute Percentage Error (MAPE) and the Coefficient of Determination (R^2), as shown in the formulas below:

$$MAPE = \frac{1}{n}\sum_{i=1}^{n}\left|\frac{y_i' - y_i}{y_i}\right| \times 100\%, \tag{3}$$

$$R^2 = 1 - \frac{\sum_{i=1}^{n}(y_i' - y_i)^2}{\sum_{i=1}^{n}(\overline{y} - y_i)^2} \tag{4}$$

where n is the number of test set sample points, y_i' is the predicted output response value for the i-th sample point, y_i is the actual output response value for the i-th sample point, and $\overline{y}$ is the average of the actual output response values for all sample points.

R^2 indicates the correlation between predicted and actual values. A value of R^2 closer to 1 signifies better performance of the surrogate model. The regression curves of the predicted versus actual output responses obtained using the surrogate model are shown in Figure 5. The results show that the regression curves of the surrogate model predictions versus actual values closely follow the ideal diagonal line, indicating good prediction accuracy. The maximum MAPE was 5.8814%, and the minimum R^2 was 0.9513. Specifically, the prediction performance for compliance in the x, y, and z directions, mass, and first-order modal frequency was excellent, with MAPE all below 3% and R^2 all above 0.99. The prediction performance for RMS and PV values of surface error in the x and y directions was slightly lower. However, since their values almost all satisfy the constraint conditions of being less than $\lambda/50$ and $\lambda/10$, respectively, this does not affect the judgment of feasibility. The prediction performance for RMS and PV values of surface error in the z direction was the poorest, but the data points near the constraint conditions were mostly clustered around the ideal diagonal line, resulting in a minimal impact on feasibility judgment. This demonstrates the effectiveness of the surrogate model, which can subsequently be used for the multi-objective optimization of the mirror's structural parameters.

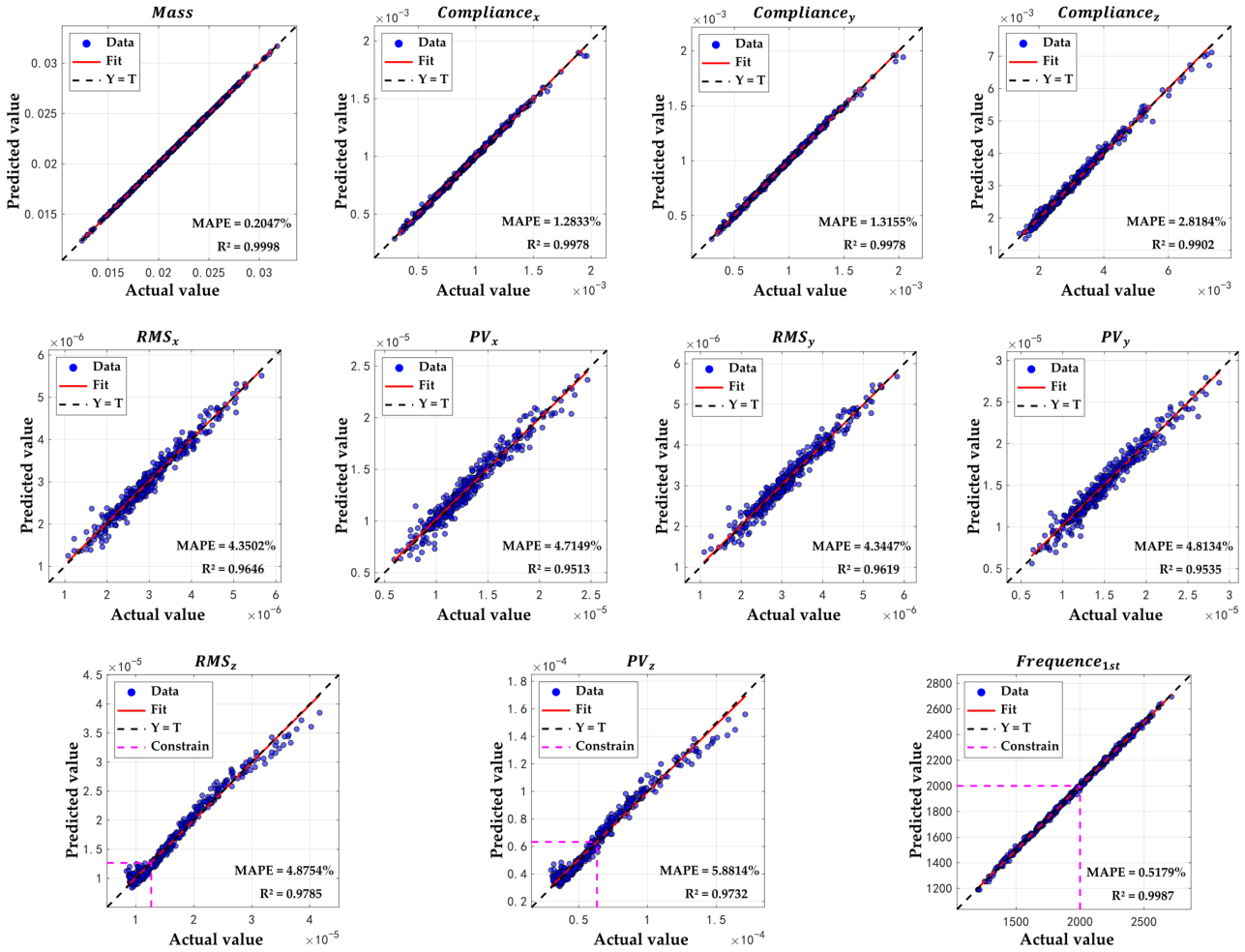


Figure 5. Regression Analysis of Predicted and Actual Values of the Surrogate Model.

3. Dynamic Constrained Success History-Based Adaptive Multi-Objective Differential Evolution Algorithm (DC-SHAMODE)

3.1. Success History-Based Adaptive Multi-Objective Differential Evolution Algorithm (SHAMODE)

SHAMODE is an advanced variant of the Differential Evolution (DE) algorithm. It incorporates an adaptive parameter control mechanism based on successful historical memory, which dynamically adjusts the mutation rate (F) and crossover rate (CR). This eliminates the need for empirical parameter tuning. This adaptive capability has been proven to be highly effective in truss structure optimization problems [32]. Therefore, this paper investigates an improved algorithm based on this method, specifically tailored for mirror structure optimization.

The SHAMODE algorithm first randomly generates an initial population N containing n individuals within the design space. It then iteratively improves the population through mutation, crossover, and selection operations. The mutation rate and crossover rate are randomly selected from the historical memory archive. The size of this archive is H, and it stores the Lehmer mean of the mutation and crossover rates corresponding to successful individuals from the most recent H iterations, thereby achieving adaptive control of the parameters. The initial values for the mutation rate and crossover rate are set to 0.5, and

the archive size H is set to 5 [23]. The update method for the historical memory archive is as follows:

$$M_{F,q} = \begin{cases} Lmean(F_s), & if \quad F_s \neq \varnothing \\ M_{F,q}, & otherwise \end{cases} \tag{5}$$

$$M_{CR,q} = \begin{cases} Lmean(CR_s), & if \quad CR_s \neq \varnothing \\ M_{CR,q}, & otherwise \end{cases} \tag{6}$$

$$q = \begin{cases} q = q+1 & if \quad q+1 \leq H \\ q = 1 & if \quad q+1 > H \end{cases} \tag{7}$$

where $M_{F,q}$ and $M_{CR,q}$ represents the mutation rate and crossover rate at position q in the historical memory archive, F_s and CR_s are the mutation rates and crossover rates corresponding to all successful individuals, respectively, $Lmean(F_s)$ and $Lmean(CR_s)$ are the Lehmer mean of the F_s and CR_s, q is the current position in the historical memory, and H is the size of the historical memory archive. During the mutation phase, the current-to-pbest/1 mutation strategy is employed to update the mutation vector:

$$v(i) = X_{iter}(i) + F_i\left(X_{pbest} - X_{iter}(i)\right) + F_i(X_{iter}(r_1) - X_{iter}(r_2)) \tag{8}$$

where $v(i)$ represents the mutation vector of individual i in population N, $X_{iter}(i)$ denotes the current position vector of individual i, X_{pbest} is a randomly selected optimal individual's position vector from the current Pareto front, $X_{iter}(r_1)$ is the position vector of individual r_1 randomly chosen from population N after excluding individual i, and $X_{iter}(r_2)$ is the position vector of individual r_2 randomly selected from the combined population of N and A after excluding individuals i and r_1. Population A is an adaptive population, initialized as an empty set with a size set to $1.4n$ [33], and is used to store successful individuals from each iteration. When the archive size is exceeded, $1.4n$ individuals are randomly selected for retention. The mutation rate F_i can be expressed as $F_i = randc_i(u_F, 0.1)$, where u_F represents a value randomly selected from the historical memory archive of mutation rates M_F, and $randc_i(u_F, 0.1)$ indicates that F_i is generated from a Cauchy distribution with mean u_F and variance 0.1, with $F_i \in [0, 1]$.

Subsequently, a crossover operation is performed between the mutation vector and the position vector to obtain the trial vector:

$$u_k(i) = \begin{cases} v_k(i) & if \quad rand \leq CR_i \quad or \quad k = k_{rand} \\ X_{iter,k}(i) & otherwise \end{cases} \tag{9}$$

where $u_k(i)$, $v_k(i)$ and $X_{iter,k}(i)$ represents the k-th dimension of the trial vector, mutation vector and current position vector of individual i, respectively, $rand$ is a random number in [0, 1], k_{rand} is a random integer in [1,D], D is the dimensionality of the design variables, and k = 1, 2, …, D. The crossover rate CR_i can be expressed as $CR_i = randn_i(u_{CR}, 0.1)$, where u_{CR} represents a value randomly selected from the historical memory archive of crossover rates M_{CR}, and $randn_i(u_{CR}, 0.1)$ indicates that CR_i is generated from a normal distribution with mean u_{CR} and variance 0.1, with $CR_i \in [0, 1]$.

Finally, the objective function values and constraint violation degree corresponding to the trial vector are calculated and compared with the individuals in the current population. Using the non-dominated sorting method of NSGA-II [34], the top n individuals are selected as the population for the next iteration. The selected trial vectors are considered successful individuals, thereby achieving iterative improvement.

3.2. Dynamic Constraint Handling Method

Compared with unconstrained multi-objective optimization problems, the presence of constraints fragments the objective space into multiple infeasible domains, thereby reducing the feasible regions to narrow or sparsely distributed areas. This can cause the population to become trapped in local feasible regions, leading to local optima. Therefore, effectively balancing the optimization objectives and constraints is key to solving constrained multi-objective optimization problems [35]. For the constrained multi-objective optimization problem of mirror structural parameters, the distribution of the 2000 sampled points in the objective function space was first plotted, with color indicating the constraint violation degree. Since the surface error under z-direction gravity is the largest, the relationship between the objective function values and the constraint violation degree was observed using RMS_z and $Frequence_{1st}$ as representatives, as shown in Figure 6. It can be seen that the constraint violation degree for RMS_z and $Frequence_{1st}$ is roughly positively correlated with the compliance objective function and negatively correlated with the mass objective function. The constrained Pareto front (CPF) is part of the unconstrained Pareto front (UPF).

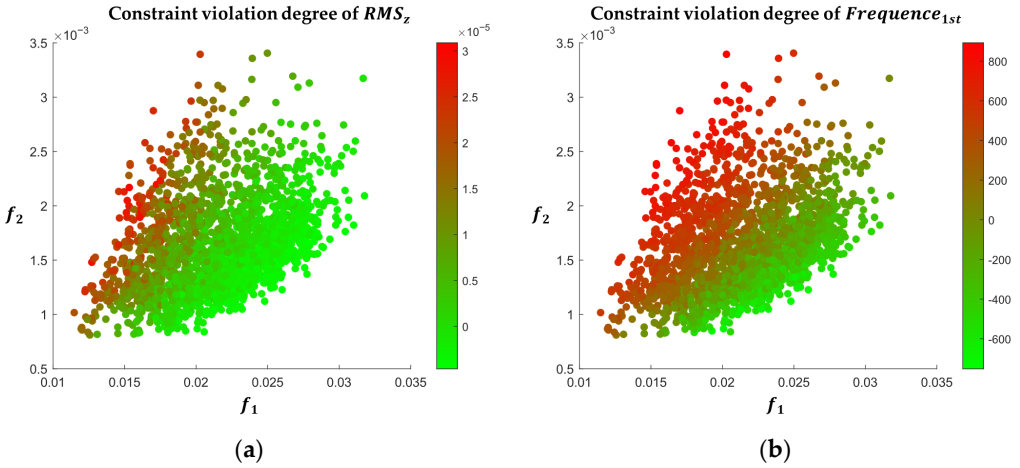


Figure 6. (**a**) Relationship between the RMS_z constraint violation degree and the objective function value; (**b**) Relationship between the $Frequence_{1st}$ constraint violation degree and the objective function value.

To better obtain the Pareto front for the mirror structural optimization problem, this paper proposes a dynamic constraint handling method. By introducing a dynamic constraint factor, the requirement for constraint violation is relaxed in the early iterations to allow faster convergence to the UPF using infeasible solutions with good objective function values. As the iterations proceed, the requirement for constraint violation is tightened to push the population into the feasible region and converge to the CPF. Since the violation degrees for different constraints in the mirror structural optimization problem differ by orders of magnitude, a dynamic constraint factor is calculated separately for each constraint:

$$\epsilon_T(k) = \epsilon_0(k) \cdot \left(1 - \frac{iter}{Maxiter}\right)^{\frac{cp \cdot iter}{Maxiter}} \tag{10}$$

$$\epsilon_0(k) = \max(Cons(k)) \quad k = 1, 2, \ldots, 7 \tag{11}$$

where $\epsilon_T(k)$ represents the dynamic constraint factor for the k-th constraint, $\epsilon_0(k)$ denotes the initial value of the dynamic constraint factor for the k-th constraint, $\max(Cons(k))$ represents the maximum value of $Cons(k)$, $Cons(k)$ represents the violation degree values of the k-th constraint for all individuals in the initial population, k is the constraint dimension,

iter is the iteration number, *Maxiter* is the maximum number of iterations, and *cp* is the decay rate control parameter. In this study, the dynamic constraint factor is adjusted to be a small value $\epsilon_\lambda(k) = 0.01 \cdot \epsilon_0(k)$ at the generation $iter_\lambda = 0.2 \cdot Maxiter$. Thus the decay rate control parameter $cp = \frac{\ln \frac{\epsilon_\lambda(k)}{\epsilon_0(k)}}{\frac{iter_\lambda}{Maxiter} \cdot \ln\left(1 - \frac{iter_\lambda}{Maxiter}\right)} = \frac{\ln 0.01}{0.2 \cdot \ln 0.8} \approx 100$. The improved non-dominated solution selection method based on dynamic constraint handling is shown in Algorithm 1:

Algorithm 1: Improved non-dominated solutions judging method

Input: $\boldsymbol{f}(\boldsymbol{x}_1), \boldsymbol{f}(\boldsymbol{x}_2), \boldsymbol{g}(\boldsymbol{x}_1), \boldsymbol{g}(\boldsymbol{x}_2)$ and $\boldsymbol{\epsilon_T}$
Output: p_1, p_2
Extract the dimension m of the objective function $\boldsymbol{f}(\boldsymbol{x}_1)$;
Extract the dimension n of the constraint violation degree $\boldsymbol{g}(\boldsymbol{x}_1)$;
For $i = 1 : n$
    If $g_i(\boldsymbol{x}_1) \leq \epsilon_T(i) \longrightarrow g_i(\boldsymbol{x}_1) = 0$;
    If $g_i(\boldsymbol{x}_2) \leq \epsilon_T(i) \longrightarrow g_i(\boldsymbol{x}_2) = 0$;
End
$g_{max1} = \max(\boldsymbol{g}(\boldsymbol{x}_1))$; $g_{max2} = \max(\boldsymbol{g}(\boldsymbol{x}_2))$;
If $g_{max1} \leq 0$ && $g_{max2} \leq 0$
    If $\boldsymbol{f}(\boldsymbol{x}_1) \leq \boldsymbol{f}(\boldsymbol{x}_2)$ in all dimensions m, and $\boldsymbol{f}(\boldsymbol{x}_1) < \boldsymbol{f}(\boldsymbol{x}_2)$ in at least one dimension
        $\boldsymbol{x}_1 \prec \boldsymbol{x}_2$, $p_1 = 1$ and $p_2 = 0$;
    Else if $\boldsymbol{f}(\boldsymbol{x}_2) \leq \boldsymbol{f}(\boldsymbol{x}_1)$ in all dimensions m, and $\boldsymbol{f}(\boldsymbol{x}_2) < \boldsymbol{f}(\boldsymbol{x}_1)$ in at least one dimension
        $\boldsymbol{x}_2 \prec \boldsymbol{x}_1$, $p_1 = 0$ and $p_2 = 1$;
    Else
        $\boldsymbol{x}_1$ and $\boldsymbol{x}_2$ are mutually non-dominating, $p_1 = 0$ and $p_2 = 0$;
    End
Else if $g_{max1} \leq 0$ && $g_{max2} > 0$
    $\boldsymbol{x}_1 \prec \boldsymbol{x}_2$, $p_1 = 1$ and $p_2 = 0$;
Else if $g_{max2} \leq 0$ && $g_{max1} > 0$
    $\boldsymbol{x}_2 \prec \boldsymbol{x}_1$, $p_1 = 0$ and $p_2 = 1$;
Else if $g_{max1} \leq g_{max2}$
    $\boldsymbol{x}_1 \prec \boldsymbol{x}_2$, $p_1 = 1$ and $p_2 = 0$;
Else
    $\boldsymbol{x}_2 \prec \boldsymbol{x}_1$, $p_1 = 0$ and $p_2 = 1$;
End

3.3. Procedure of DC-SHAMODE

The DC-SHAMODE algorithm proposed in this paper improves the selection of successful individuals in SHAMODE by utilizing a dynamic constraint handling method. It fully leverages the information from infeasible solutions in the early iterations, thereby enhancing convergence. The main procedure of the algorithm is as follows:

Step 1: Define the optimization problem. Randomly generate the position vectors of the initial population within the solution space, calculate the corresponding objective function values and constraint violation degrees. Use the non-dominated sorting method to extract the Pareto front of the initial population as the initial Pareto archive. Calculate the initial dynamic constraint factors using Equation (11) and initialize the historical memory archive.

Step 2: Enter the main algorithm loop. Calculate the dynamic constraint factors for the current iteration using Equation (10). Randomly select the mean mutation rate u_F and the mean crossover rate u_{CR} for this iteration from the historical memory archive.

Generate the mutation rate and crossover rate for each individual by sampling from a Cauchy distribution and a normal distribution (both with a variance of 0.1), respectively.

Step 3: Compute the mutation vectors using Equation (8) and enforce boundary control on them.

Step 4: Compute the trial vectors using Equation (9) and calculate their corresponding objective function values and constraint violation degrees.

Step 5: Merge the parent population archive with the trial vector archive. Generate the offspring population archive using the improved non-dominated sorting method based on dynamic constraint handling, and record the indices of the successful individuals.

Step 6: Update the mutation rates and crossover rates using Equations (5) and (6), applying boundary control. Then, update the historical memory position using Equation (7). Merge the successful individuals into the adaptive archive, control its size, and complete the update of the historical memory archive.

Step 7: Merge the Pareto archive with the trial vector archive. Extract a new Pareto front using the non-dominated sorting method to serve as the updated Pareto archive, controlling its size.

Step 8: If the stopping criterion (maximum number of iterations) is not met, return to Step 2 to continue the iteration. Otherwise, exit the main loop and output the Pareto archive as the final Pareto front for the solved multi-objective optimization problem.

The flowchart and pseudocode of the dC-SHAMODE algorithm are shown in Figure 7 and Algorithm 2, respectively.

Algorithm 2: Pseudo-code of DC-SHAMODE

Randomly generate the position vectors of the initial population $\boldsymbol{X_0}$, and calculate the corresponding objective function values and constraint violation degrees;
$\boldsymbol{Pareto_0}$ = non-dominated individual in $\boldsymbol{X_0}$ obtained by the non-dominated sorting method;
Calculate the initial value $\boldsymbol{\epsilon_0}$ of the dynamic constraint factor using Equation (11), and initialize the historical memory archive;
For iter = 1: Maxiter
    Calculate the mutation rate $\boldsymbol{F}$ and crossover rate $\boldsymbol{CR}$;
    Calculate the mutation vector $\boldsymbol{v}$ by Equation (8) and control the boundaries;
    Calculate the trial vector $\boldsymbol{u}$ using Equation (9)
    Calculate the objective values and constraint violation degrees for each individual;
    Calculate the dynamic constraint factor $\boldsymbol{\epsilon_T}$ by Equation (10);
    $\boldsymbol{X_{iter+1}}$ = best nsol individuals in $\boldsymbol{X_{iter}} \cup \boldsymbol{u}$ with highest non-dominated levels, obtained by the improved non-dominated sorting method based on dynamic constraint;
    $\boldsymbol{S}$ = set of indices of $\boldsymbol{u}$ that survived and are included in $\boldsymbol{X_{iter+1}}$;
    $\boldsymbol{A_{iter+1}} = \boldsymbol{A_{iter}} \cup \boldsymbol{u_S}$;
    $\boldsymbol{Pareto_{iter+1}}$ = non-dominated individual in $\boldsymbol{Pareto_{iter}} \cup \boldsymbol{u}$ obtained by the non-dominated sorting method;
    Calculate the cell of historical memories $M_{F,q}$ and $M_{CR,q}$ by Equations (5) and (6);
    Update the historical memory location counter q using Equation (7);
    Record the pareto solutions;
End

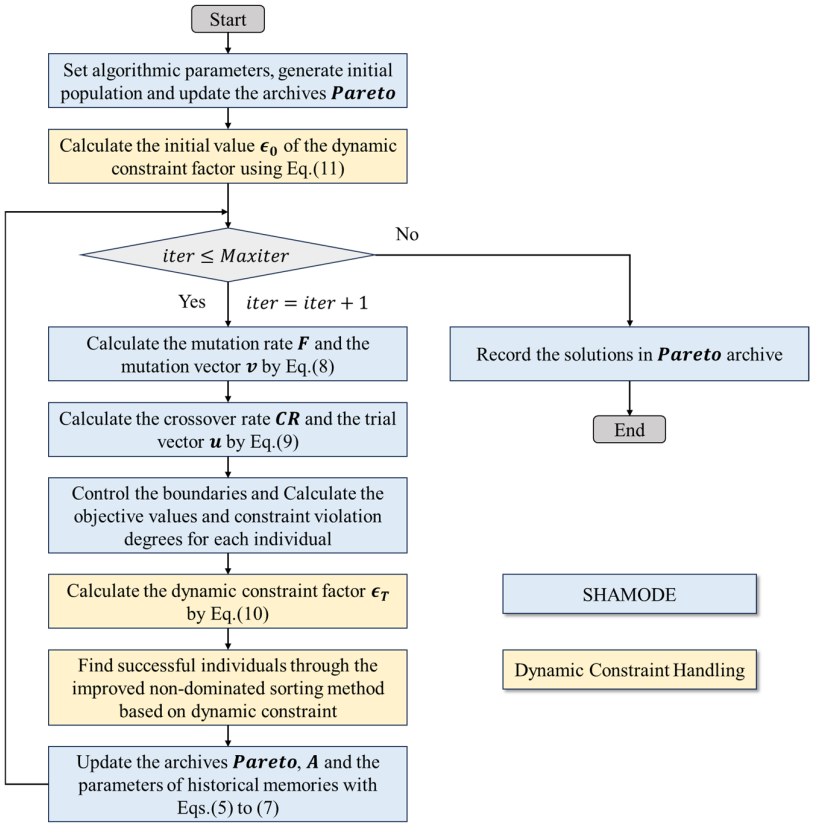


Figure 7. Flowchart of DC-SHAMODE.

4. Results and Discussion

To evaluate the performance of the proposed DC-SHAMODE algorithm in the multi-objective optimization of mirror structural parameters, it was compared with 13 other advanced constrained multi-objective optimization algorithms: APSEA [12], cDPEA [13], DVCEA [14], tDEACPBI [15], EMCMO [17], CMOEACD [18], SHAMODE [23], SHAMODE-WO [24], MO-SHADE-MRFO [25], CCMO [36], CMOEAMS [37], NSGAII [34], and NS-GAIII [38]. For all algorithms, the population size was set to 100, the maximum number of iterations was 10,000, and each algorithm was independently run 30 times.

4.1. Algorithm Performance Evaluation

To compare the performance of different algorithms, three distinct metrics were employed for evaluation: Hypervolume (HV), Generational Distance (GD), and Spacing. Hypervolume (HV) is used to measure the region covered by the generated Pareto front solution set. It is defined as the volume between a reference point representing the worst-case solution and the Pareto front, as shown in Equation (12):

$$HV = \bigcup_{i=1}^{P} V_i \tag{12}$$

where P represents the number of solutions in the Pareto front, and V_i denotes the hypervolume contributed by the i-th non-dominated solution relative to the reference point. When the HV value is larger, it implies that the Pareto front generated by the algorithm spans a wider area within the objective function domain.

Generational Distance (GD) is used to measure the distance between the generated Pareto front and a reference front. It is defined as the average distance from each solution in the Pareto front to its nearest solution on the reference front, as shown in Equation (13):

$$GD = \frac{\sqrt{\sum_{i=1}^{P} (d_i)^2}}{P} \tag{13}$$

where d_i represents the Euclidean distance from the i-th non-dominated solution in the Pareto front to the nearest solution on the reference front, and P represents the number of solutions in the Pareto front. A smaller GD value indicates that the Pareto front solution set generated by the algorithm is closer to the reference front, thereby demonstrating better convergence performance.

Spacing is used to measure the uniformity of distribution within the generated Pareto front solution set. It is defined as the standard deviation of the distances between each solution in the Pareto front and its nearest neighboring solution, as shown in Equation (14).

$$Spacing = \frac{\sqrt{\sum_{i=1}^{P} \left(d_i' - \overline{d}\right)^2}}{P-1} \tag{14}$$

where d_i' denotes the Euclidean distance from the i-th non-dominated solution in the Pareto front to its nearest neighbor within the same Pareto front, $\overline{d}$ represents the average distance from all Pareto front solutions to their respective nearest neighbors, and P represents the number of solutions in the Pareto front. A smaller $Spacing$ value indicates a more uniform distribution of the Pareto front solution set generated by the algorithm.

Since the true Pareto front for the multi-objective optimization problem of mirror structural parameters studied in this paper is unknown, a reference front was constructed by merging all Pareto front solution sets obtained from all runs of all algorithms. The non-dominated sorting method was then applied to extract the top 100 non-dominated solutions as the reference front solution set. The reference point was selected as the worst-case solution from all runs across all algorithms. The mean values and standard deviations of the three evaluation metrics and runtime obtained from repeated runs of each algorithm are presented in Table 3, the box plots of the three evaluation metrics and runtime are shown in Figure 8, and the resulting Pareto fronts are illustrated in Figure 9.

Table 3. Mean values and standard deviations of evaluation metrics and runtime.

Algorithm	HV	GD	Spacing	Runtime *
APSEA	9.8919×10^{-1} (1.15×10^{-4})	3.6032×10^{-1} (7.59×10^{-2})	1.8476×10^{-5} (1.11×10^{-5})	1.8861×10^{2} (6.07×10^{1})
cDPEA	9.8919×10^{-1} (9.28×10^{-5})	4.5135×10^{-1} (9.22×10^{-2})	3.7553×10^{-5} (3.54×10^{-5})	1.3134×10^{2} (5.83×10^{-1})
DVCEA	9.8938×10^{-1} (9.55×10^{-5})	2.4667×10^{-1} (4.81×10^{-2})	1.9551×10^{-5} (1.20×10^{-5})	2.5063×10^{2} (5.70×10^{-1})
tDEACPBI	9.8922×10^{-1} (8.31×10^{-5})	3.8604×10^{-1} (7.70×10^{-2})	2.3070×10^{-5} (1.66×10^{-5})	1.2982×10^{2} (3.84×10^{-1})
EMCMO	9.8904×10^{-1} (1.23×10^{-4})	4.7576×10^{-1} (1.03×10^{-1})	2.9613×10^{-5} (1.60×10^{-5})	2.3245×10^{2} **(3.46×10^{-1})**
CMOEACD	9.8943×10^{-1} **(4.47×10^{-5})**	3.2730×10^{-1} (3.94×10^{-2})	4.1619×10^{-5} (2.75×10^{-5})	3.4879×10^{2} (7.04×10^{-1})
CCMO	9.8909×10^{-1} (1.56×10^{-4})	4.3738×10^{-1} (9.58×10^{-2})	2.7170×10^{-5} (2.10×10^{-5})	2.3254×10^{2} (6.07×10^{-1})
CMOEAMS	9.8918×10^{-1} (1.06×10^{-4})	3.6120×10^{-1} (5.40×10^{-2})	1.5789×10^{-5} (9.21×10^{-6})	1.2923×10^{2} (5.43×10^{-1})
NSGA-II	9.8923×10^{-1} (8.97×10^{-5})	3.5211×10^{-1} (5.96×10^{-2})	1.7433×10^{-5} (1.29×10^{-5})	1.2899×10^{2} (4.37×10^{-1})
NSGA-III	9.8915×10^{-1} (9.56×10^{-5})	4.2036×10^{-1} (9.12×10^{-2})	2.5729×10^{-5} (2.00×10^{-5})	**1.2880×10^{2}** (4.77×10^{-1})
SHAMODE	9.8940×10^{-1} (5.24×10^{-5})	2.8126×10^{-1} (3.18×10^{-2})	1.9352×10^{-5} (8.38×10^{-6})	1.2900×10^{2} (5.58×10^{-1})
SHAMODE-WO	9.8942×10^{-1} (7.26×10^{-5})	2.5439×10^{-1} (2.17×10^{-2})	1.7058×10^{-5} (9.84×10^{-6})	1.3538×10^{2} (1.72×10^{1})
MO-SHADE-MRFO	9.8892×10^{-1} (1.89×10^{-4})	5.5207×10^{-1} (1.30×10^{-1})	6.3218×10^{-5} (4.96×10^{-5})	1.3444×10^{2} (1.06×10^{1})
DC-SHAMODE	**9.8947×10^{-1}** (5.33×10^{-5})	**2.1308×10^{-1} (2.88×10^{-2})**	**1.1646×10^{-6} (4.99×10^{-6})**	1.3014×10^{2} (5.06×10^{-1})

* The runtime is in seconds (computer specs: Intel Core i7 13700KF, 64 GB RAM, RTX 3060Ti), and the three evaluation metrics HV, GD, and Spacing are all dimensionless relative metrics. Bold values indicate the best results for each corresponding index.

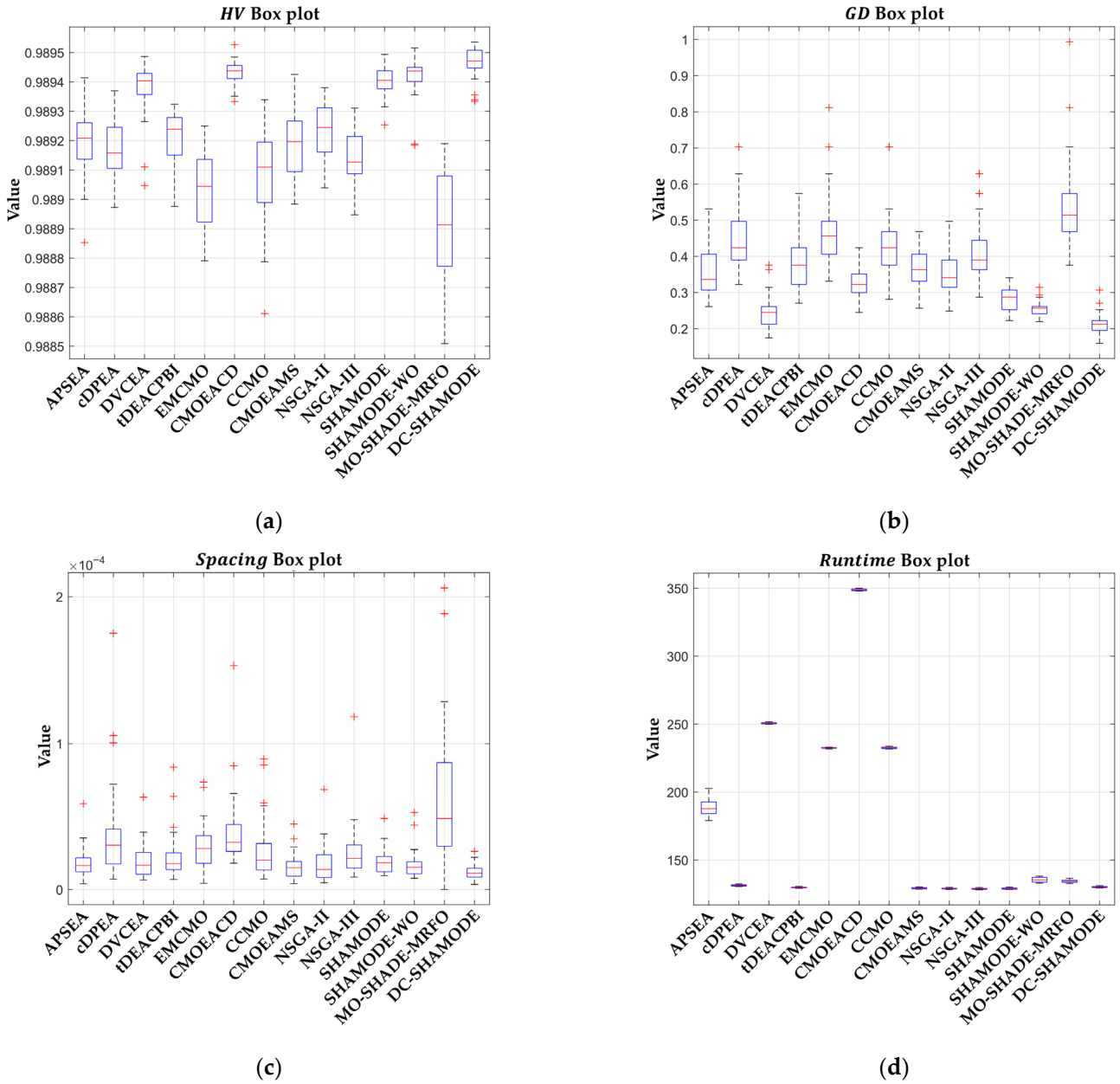


Figure 8. (**a**) Box plots of HV evaluation metrics; (**b**) Box plots of GD evaluation metrics; (**c**) Box plots of Spacing evaluation metrics; (**d**) Box plots of runtime.

The results indicate that the proposed DC-SHAMODE algorithm achieved the best Pareto front among all compared algorithms. Although its runtime is slightly longer than that of tDEACPBI, CMOEAMS, NSGA-II, NSGA-III, and SHAMODE, the difference is small. Meanwhile, it obtains the best mean values and favorable standard deviations across all three evaluation metrics. This demonstrates that the proposed algorithm exhibits good convergence and diversity, along with strong consistency across repeated runs. It proves that for the multi-objective optimization problem of mirror structural parameters, the proposed algorithm, enhanced by incorporating a dynamic constraint handling mechanism into the success history-based adaptive multi-objective differential evolution algorithm, can improve the convergence of the Pareto front solution set while preserving the diversity of its distribution.

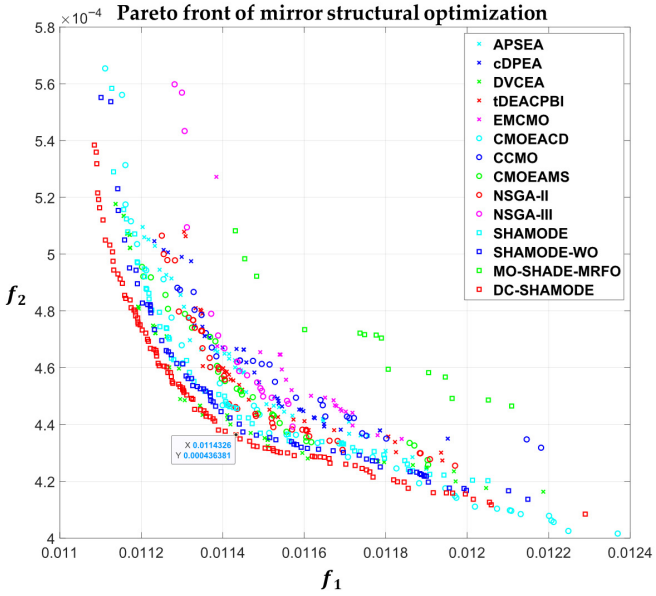
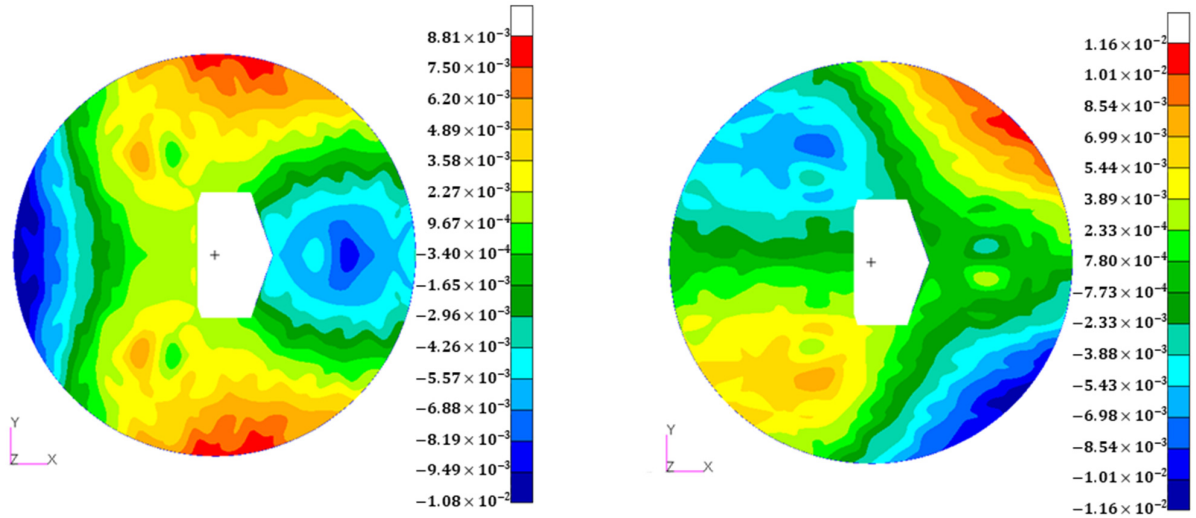


Figure 9. Pareto front of multi-objective optimization for mirror structural parameters.

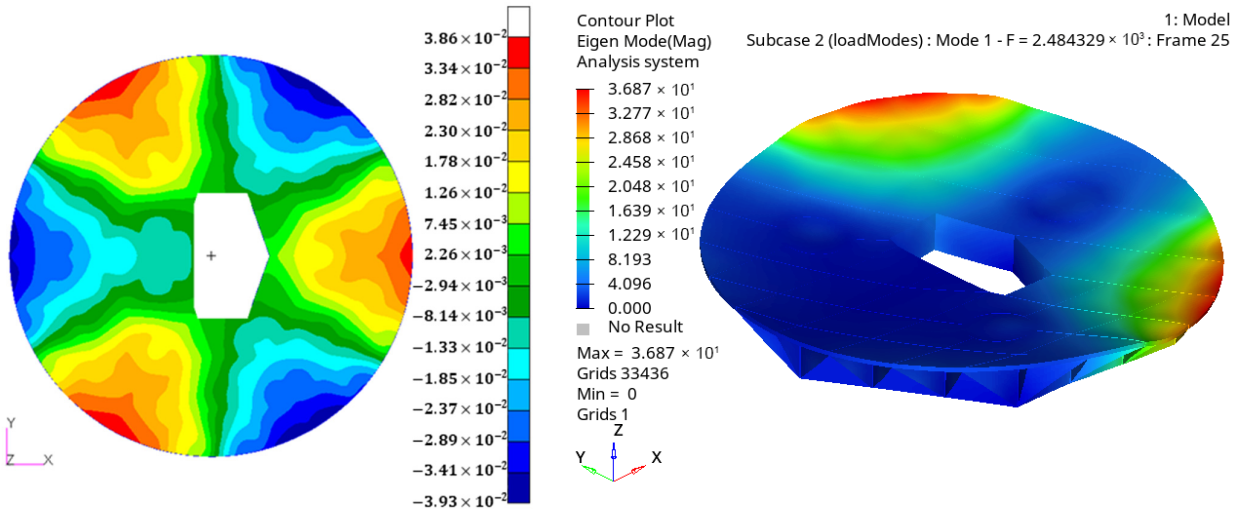
4.2. Optimization Results Analysis

From the Pareto front obtained by the DC-SHAMODE algorithm, a solution with a relatively balanced trade-off between mass and compliance was selected based on empirical judgment as the optimization result for the mirror's structural parameters, as shown in Figure 9. To facilitate the manufacturing of the mirror, the structural dimensional parameters corresponding to the optimization result were adjusted and rounded to practical values, yielding the final values for each design variable. These final values were input into the integrated simulation linkage to obtain the optical performance and first-order mode shape corresponding to the final optimized design of the mirror structure, as shown in Figure 10. The initial, optimized, and final values for each design variable are listed in Table 4, where the output responses for the initial and final values are simulation results, while those for the optimized value are predictions from the surrogate model.



(**a**) (**b**)

Figure 10. *Cont.*



(**c**) (**d**)

Figure 10. (**a**) Surface error of the final mirror structure in the x-direction; (**b**) Surface error of the final mirror structure in the y-direction; (**c**) Surface error of the final mirror structure in the z-direction; (**d**) First-order mode shape of the final mirror structure.

Table 4. Comparison of initial, optimized and final values of design variables and corresponding output response results.

Parameter *	Initial Design	Optimized Design	Final Design
x_1	2.5000	2.0539	2.1000
x_2	2.5000	2.0006	2.0000
x_3	2.5000	4.1465	4.1000
x_4	2.5000	2.0034	2.0000
x_5	2.5000	2.0001	2.0000
x_6	2.5000	3.7715	3.8000
x_7	2.5000	2.6868	2.7000
x_8	2.5000	2.0090	2.0000
x_9	2.5000	2.0208	2.0000
x_{10}	12.0000	6.4005	6.4000
x_{11}	12.0000	3.3238	3.3000
x_{12}	12.0000	12.0377	12.0000
x_{13}	12.0000	3.0010	3.0000
x_{14}	5.0000	3.0017	3.0000
x_{15}	10.0000	10.0482	10.0000
x_{16}	110.0000	94.1130	94.1000
x_{17}	10.0000	14.9562	15.0000
x_{18}	10.0000	14.8905	14.9000
x_{19}	10.0000	14.9749	15.0000
x_{20}	10.0000	14.9996	15.0000
x_{21}	10.0000	14.7436	14.7000
$Mass$	16.8105	11.4326	11.3972
$Compliance_x$	6.3040×10^{-4}	2.7981×10^{-4}	2.6260×10^{-4}
$Compliance_y$	6.3862×10^{-4}	2.7187×10^{-4}	2.6152×10^{-4}
$Compliance_z$	1.7053×10^{-3}	7.5746×10^{-4}	8.1564×10^{-4}
RMS_x	2.9552×10^{-6}	2.9680×10^{-6}	2.7705×10^{-6}
PV_x	1.3026×10^{-5}	1.3136×10^{-5}	1.2410×10^{-5}

Table 4. *Cont.*

Parameter *	Initial Design	Optimized Design	Final Design
RMS_y	3.0947×10^{-6}	3.0130×10^{-6}	2.8108×10^{-6}
PV_y	1.4732×10^{-5}	1.5653×10^{-5}	1.4739×10^{-5}
RMS_z	1.2567×10^{-5}	1.2632×10^{-5}	1.1859×10^{-5}
PV_z	4.7487×10^{-5}	5.2533×10^{-5}	4.9325×10^{-5}
$Frequence_{1st}$	2306.8890	2464.9252	2484.3290

* All input design variables x_1~x_{21} are in mm. For the output responses, the objective function *Mass* is in kg, and $Compliance_x$, $Compliance_y$, $Compliance_z$ is in N·mm. The surface error *RMS* and *PV* values are in mm, and the $Frequence_{1st}$ is in Hz.

The results indicate that the final optimized design satisfies all constraint requirements. Compared to the initial design, the mass is reduced from 16.8105 kg to 11.3972 kg, achieving a lightweighting rate of 32.2%. Concurrently, the $Compliance_x$ value decreases from 6.3040×10^{-4} N·mm to 2.6260×10^{-4} N·mm, $Compliance_y$ from 6.3862×10^{-4} N·mm to 2.6152×10^{-4} N·mm, and $Compliance_z$ from 1.7053×10^{-3} N·mm to 8.1564×10^{-4} N·mm, representing reductions of 58.3%, 59.05%, and 52.17%, respectively. The RMS_x value decreases from 2.9552 nm to 2.7705 nm (a reduction of 6.25%), and PV_x decreases from 13.026 nm to 12.410 nm (a reduction of 4.73%). The RMS_y value decreases from 3.0947 nm to 2.8108 nm (a reduction of 9.17%), while PV_y slightly increases from 14.732 nm to 14.739 nm (an increase of 0.05%). The RMS_z value decreases from 12.567 nm to 11.859 nm (a reduction of 5.63%), whereas PV_z increases from 47.487 nm to 49.325 nm (an increase of 3.87%). The $Frequence_{1st}$ value increases from 2306.889 Hz to 2484.329 Hz (an improvement of 7.69%). Although the surface error PV values under gravity in the y and z directions show a slight increase, the overall RMS values of the mirror surface error are all reduced. Furthermore, the compliance in all three directions is significantly decreased. Combined with the increase in the first-order modal frequency, these results demonstrate a clear enhancement in the structural stiffness of the mirror. This proves that applying the DC-SHAMODE algorithm for the multi-objective optimization of the mirror's structural parameters can effectively reduce the mirror's mass while simultaneously improving structural stiffness, ensuring surface accuracy requirements are met, and increasing the fundamental frequency.

5. Conclusions

To address the conflicting requirements between mass and stiffness in the lightweight design of space camera mirrors, this study focused on a 700 mm aperture primary mirror of a space camera. A success history-based adaptive multi-objective differential evolution algorithm with dynamic constraints (DC-SHAMODE) was proposed. By analyzing the relationship between the mirror's surface error and first-order modal frequency constraints and the objective functions of mass and compliance, improvements were made to the SHAMODE algorithm through the introduction of a constraint dynamic adjustment mechanism. This mechanism helps to fully utilize infeasible solutions with favorable objective function values in the early stages of iteration, guiding the population towards rapid convergence to the UPF. As iterations progress, the requirement for constraint violation is gradually tightened, ultimately driving the population into the feasible region and converging to the CPF. Concurrently, to enhance optimization efficiency, a surrogate model for the mirror was constructed using the Kriging algorithm, establishing a mapping relationship between input variables and output responses. This approach effectively reduces the computational time and resources required while maintaining the prediction accuracy of the output responses. Through comparison with 13 different multi-objective optimization algorithms, the proposed algorithm demonstrates its capability to improve the convergence of the Pareto front solution set while preserving the diversity of its distri-

bution. This verifies its effectiveness in handling the multi-objective optimization of mirror structural parameters.

Finally, a solution with a balanced trade-off between mass and compliance was selected from the Pareto front obtained by the proposed algorithm. The corresponding structural dimensions were adjusted according to manufacturing constraints to derive the final optimized design, which was subsequently subjected to simulation analysis. The results show that, compared to the initial mirror structure, the final structure significantly reduces compliance by 58.3%, 59.05%, and 52.17% in the x, y, and z directions, respectively, while ensuring that surface accuracy and first-order modal frequency meet the constraint requirements. Furthermore, the mass is reduced from 16.8105 kg to 11.3972 kg, achieving a lightweighting rate of 32.2%.

In this paper, a dynamic constraint adjustment mechanism is innovatively introduced based on the SHAMODE algorithm, which overcomes the limitations of traditional fixed constraint handling strategies and realizes the full utilization of infeasible solutions in the early stage of iteration. Furthermore, by integrating the Kriging surrogate model with the improved evolutionary algorithm, a high-efficiency optimization framework is constructed to solve the problem of high computational cost of finite element analysis in the lightweight design of space camera mirrors. Despite the promising results, this study has certain limitations. The primary limitation is the dependence on the accuracy of the constructed Kriging surrogate model. Since the accuracy of the surrogate model depends on the sampling quality and the distribution of training data, this may affect the robustness of optimization in highly nonlinear regions. Furthermore, the current optimization framework primarily considers static and modal performances under idealized on-ground conditions, without fully accounting for the coupled effects of a space environment, such as thermal deformation in orbit or dynamic responses during the launch process.

Future work will focus on addressing these limitations, including exploring more advanced surrogate models such as adaptive sampling strategies or deep neural networks to further improve prediction accuracy; incorporating multi-physics coupling constraints, including thermo-elastic and random vibration analysis, into the optimization model, and validating the proposed method through practical engineering applications. In summary, the proposed DC-SHAMODE algorithm demonstrates strong competitiveness in solving multi-objective optimization problems for mirror structural parameters. The established multi-objective optimization design framework offers valuable references for the lightweight design of similar space camera mirrors.

Supplementary Materials: The following supporting information can be downloaded at: https://www.mdpi.com/article/10.3390/photonics13030283/s1, Finite element models for static analysis and modal analysis.

Author Contributions: Conceptualization, J.T. and W.X.; methodology, J.T. and Q.Y.; software, J.T.; validation, J.T. and Q.Y.; formal analysis, Q.Y.; investigation, J.T. and S.Z.; resources, W.X. and L.C.; data curation, S.Z.; writing—original draft preparation, J.T.; writing—review and editing, Q.Y.; visualization, J.T. and Q.Y.; supervision, W.X., S.Z. and L.C.; project administration, W.X., S.Z. and L.C.; funding acquisition, L.C. All authors have read and agreed to the published version of the manuscript.

Funding: This research was funded by the Natural Science Foundation of Jilin Province, grant number 20250102177JC.

Institutional Review Board Statement: Not applicable.

Informed Consent Statement: Not applicable.

Data Availability Statement: The data that support the findings of this study are available from the corresponding author upon reasonable request.

Conflicts of Interest: The authors declare no conflicts of interest.

References

1. Dun, X.; Zhang, J.; Chen, F.; Zhang, Z.; Wang, X.; Xing, Y.; Dong, S.; Fan, Z.; Shi, Y.; Gordon, W.; et al. Neural array meta-imaging. *eLight* **2025**, *5*, 33. [CrossRef]
2. Jia, P.; Tian, D.; Wang, Y.; Yao, D.; Xu, R.; Sun, J.; Sun, H.; Zhang, B. Airborne optical imaging technology: A road map in CIOMP. *Light Sci. Appl.* **2025**, *14*, 119. [CrossRef]
3. Zhang, X.; Sun, L.; Qi, L. Bayesian Regularization Algorithm Based Recurrent Neural Network Method and NSGA-II for the Optimal Design of the Reflector. *Machines* **2022**, *10*, 63. [CrossRef]
4. Wang, Z.; Zhang, J.; Wang, J.; He, X.; Fu, L.; Tian, F.; Liu, X.; Zhao, Y. A Back Propagation neural network based optimizing model of space-based large mirror structure. *Optik* **2019**, *179*, 780–786. [CrossRef]
5. Liu, X.; Gu, K.; Li, M.; Cheng, Z. Optimization Design of Large-Aperture Primary Mirror for a Space Remote Camera. *Sensors* **2023**, *23*, 5441. [CrossRef] [PubMed]
6. Wang, H.; Guo, J.; Shao, M.; Sun, J.; Tian, F.; Yang, X. Optimization design of an ultralight large-aperture space mirror. *Appl. Opt.* **2021**, *60*, 10878. [CrossRef] [PubMed]
7. Liu, G.; Guo, L.; Wang, X.; Wu, Q. Topology and parametric optimization based lightweight design of a space reflective mirror. *Opt. Eng.* **2018**, *57*, 075101. [CrossRef]
8. Dong, Q.; Wang, Q.; Wang, C.; Luan, Y.; Wang, X.; Wang, X. Multiobjective Optimization of SiC Mirror Based on Dual-Parameter Coupling. *Photonics* **2023**, *10*, 171. [CrossRef]
9. Sun, L.; Zhang, B.; Wang, P.; Gan, Z.; Han, P.; Wang, Y. Multi-Objective Parametric Optimization Design for Mirrors Combined with Non-Dominated Sorting Genetic Algorithm. *Appl. Sci.* **2023**, *13*, 3346. [CrossRef]
10. Qin, T.; Guo, J.; Jing, Z.; Han, P.; Qi, B. Hybrid IPSO-IAGA-BPNN algorithm-based rapid multi-objective optimization of a fully parameterized spaceborne primary mirror. *Appl. Opt.* **2021**, *60*, 3031. [CrossRef]
11. Hu, M.; Huang, G.; Yang, X.; Xiao, J.; Wang, X.; Zhang, T. From penalty function to learning-driven: Evolution and perspectives of constrained multi-objective evolutionary algorithm. *Swarm Evol. Comput.* **2025**, *96*, 102006. [CrossRef]
12. Tian, Y.; Wang, R.; Zhang, Y.; Zhang, X. Adaptive population sizing for multi-population based constrained multi-objective optimization. *Neurocomputing* **2025**, *621*, 129296. [CrossRef]
13. Ming, M.; Trivedi, A.; Wang, R.; Srinivasan, D.; Zhang, T. A Dual-Population-Based Evolutionary Algorithm for Constrained Multiobjective Optimization. *IEEE Trans. Evol. Comput.* **2021**, *25*, 739–753. [CrossRef]
14. Ban, X.; Liang, J.; Qiao, K.; Yu, K.; Wang, Y.; Peng, J.; Qu, B. A Decision Variables Classification-Based Evolutionary Algorithm for Constrained Multi-Objective Optimization Problems. *IEEE/CAA J. Autom. Sin.* **2025**, *12*, 1830–1849. [CrossRef]
15. Ming, F.; Gong, W.; Wang, L.; Gao, L. A Constraint-Handling Technique for Decomposition-Based Constrained Many-Objective Evolutionary Algorithms. *IEEE Trans. Syst. Man Cybern. Syst.* **2023**, *53*, 7783–7793. [CrossRef]
16. Qiao, K.; Yu, K.; Yue, C.; Qu, B.; Liu, M.; Liang, J. A Cooperative Multistep Mutation Strategy for Multiobjective Optimization Problems with Deceptive Constraints. *IEEE Trans. Syst. Man Cybern. Syst.* **2024**, *54*, 6670–6682. [CrossRef]
17. Qiao, K.; Yu, K.; Qu, B.; Liang, J.; Song, H.; Yue, C. An Evolutionary Multitasking Optimization Framework for Constrained Multiobjective Optimization Problems. *IEEE Trans. Evol. Comput.* **2022**, *26*, 263–277. [CrossRef]
18. Liu, Z.; Han, F.; Ling, Q.; Han, H.; Jiang, J. Constraint-Pareto Dominance and Diversity Enhancement Strategy-Based Evolutionary Algorithm for Solving Constrained Multiobjective Optimization Problems. *IEEE Trans. Evol. Comput.* **2025**, *29*, 2771–2784. [CrossRef]
19. Zhang, D.; Wang, L.; Qiao, K.; Yu, K.; Li, Y. A multi-population evolutionary algorithm based on constraint grouping for constrained multiobjective optimization problems. *Expert Syst. Appl.* **2026**, *295*, 128830. [CrossRef]
20. Li, Z.; Liu, Z.; Su, C. A multi-stage evolutionary algorithm based on finite state machine theory for constrained multi-objective optimization problem. *Swarm Evol. Comput.* **2026**, *100*, 102222. [CrossRef]
21. Wolpert, D.H.; Macready, W.G. No free lunch theorems for optimization. *IEEE Trans. Evol. Comput.* **1997**, *1*, 67–82. [CrossRef]
22. Tanabe, R.; Fukunaga, A. Success-History Based Parameter Adaptation for Differential Evolution. In *2013 IEEE Congress on Evolutionary Computation*; IEEE: New York, NY, USA, 2013; pp. 71–78.
23. Panagant, N.; Bureerat, S.; Tai, K. A novel self-adaptive hybrid multi-objective meta-heuristic for reliability design of trusses with simultaneous topology, shape and sizing optimisation design variables. *Struct. Multidiscip. Optim.* **2019**, *60*, 1937–1955. [CrossRef]
24. Zhong, C.; Li, G.; Meng, Z.; Li, H.; He, W. Multi-objective SHADE with manta ray foraging optimizer for structural design problems. *Appl. Soft Comput.* **2023**, *134*, 110016. [CrossRef]

25. Anosri, S.; Panagant, N.; Bureerat, S.; Pholdee, N. Success history based adaptive multi-objective differential evolution variants with an interval scheme for solving simultaneous topology, shape and sizing truss reliability optimisation. *Knowl. Based Syst.* **2022**, *253*, 109533. [CrossRef]
26. Yuan, J.; Zhang, L. Structure design and verification of primary mirror assembly for large off-axis TMA camera. *Infrared Laser Eng.* **2023**, *52*, 20220363.
27. Bao, Q.H.; Sha, W.; Chen, C.Z.; Ren, J. Lightweight and optimization design of rectangular reflective mirror supported in centre. *Infrared Laser Eng.* **2017**, *46*, 718003. [CrossRef]
28. Samadian, D.; Muhit, I.B.; Dawood, N. Application of Data-Driven Surrogate Models in Structural Engineering: A Literature Review. *Arch. Comput. Methods Eng.* **2024**, *32*, 735–784. [CrossRef]
29. Park, J.S. Optimal Latin-hypercube designs for computer experiments. *J. Stat. Plan. Inference* **1994**, *39*, 95–111. [CrossRef]
30. Krige, D.G. A statistical approach to some basic mine valuation problems on the Witwatersrand. *J. S. Afr. Inst. Min. Metall.* **1951**, *52*, 119–139.
31. Kudela, J.; Matousek, R. Recent advances and applications of surrogate models for finite element method computations: A review. *Soft Comput.* **2022**, *26*, 13709–13733. [CrossRef]
32. Panagant, N.; Pholdee, N.; Bureerat, S.; Yildiz, A.R.; Mirjalili, S. A Comparative Study of Recent Multi-objective Metaheuristics for Solving Constrained Truss Optimisation Problems. *Arch. Comput. Methods Eng.* **2021**, *28*, 4031–4047. [CrossRef]
33. Tanabe, R.; Fukunaga, A.S. Improving the Search Performance of SHADE Using Linear Population Size Reduction. In *2014 IEEE Congress on Evolutionary Computation (CEC)*; IEEE: New York, NY, USA, 2014; pp. 1658–1665.
34. Deb, K.; Pratap, A.; Agarwal, S.; Meyarivan, T.A.M.T. A fast and elitist multiobjective genetic algorithm: NSGA-II. *IEEE Trans. Evol. Comput.* **2002**, *6*, 182–197. [CrossRef]
35. Chen, M.; Zhao, S.; Zhang, T.; Zhang, L. A dual-population based two-archive coevolution algorithm for constrained multi-objective optimization problems. *Eng. Appl. Artif. Intell.* **2025**, *158*, 111419. [CrossRef]
36. Tian, Y.; Zhang, T.; Xiao, J.; Zhang, X.; Jin, Y. A Coevolutionary Framework for Constrained Multiobjective Optimization Problems. *IEEE Trans. Evol. Comput.* **2021**, *25*, 102–116. [CrossRef]
37. Tian, Y.; Zhang, Y.; Su, Y.; Zhang, X.; Tan, K.C.; Jin, Y. Balancing Objective Optimization and Constraint Satisfaction in Constrained Evolutionary Multiobjective Optimization. *IEEE Trans. Cybern.* **2022**, *52*, 9559–9572. [CrossRef]
38. Deb, K.; Jain, H. An Evolutionary Many-Objective Optimization Algorithm Using Reference-Point-Based Nondominated Sorting Approach, Part I: Solving Problems with Box Constraints. *IEEE Trans. Evol. Comput.* **2014**, *18*, 577–601. [CrossRef]

Disclaimer/Publisher's Note: The statements, opinions and data contained in all publications are solely those of the individual author(s) and contributor(s) and not of MDPI and/or the editor(s). MDPI and/or the editor(s) disclaim responsibility for any injury to people or property resulting from any ideas, methods, instructions or products referred to in the content.